Freshwater plume detection and volumetric estimation offshore Hawai‘i using marine electromagnetic imaging

Eric Attias[1], Steven Constable[2], Dallas Sherman[3], Khaira Ismail[4], Christopher Shuler[1] and Henrietta Dulai[1]

[1]Hawai‘i Institute of Geophysics and Planetology, School of Ocean and Earth Science and Technology, University of Hawai‘i at Mānoa, HI, USA.

[2]Scripps Institution of Oceanography, University of California San Diego, CA, USA.

[3]Frontier Geosciences, BC, Canada.

[4]Universiti Malaysia Terrengganu, Malaysia.

Key Points:

- Surface-towed marine-controlled source electromagnetic technique is capable of imaging freshwater plumes in high-resolution
- Multiple large-scale freshwater plumes and surface freshwater bodies were detected offshore the island of Hawai‘i
- Substantial volumes of freshwater occupy seafloor to ocean surface plumes in the west of Hawai‘i

Corresponding author: Eric Attias, `attias@hawaii.edu`

Abstract

Submarine groundwater discharge (SGD) is an important phenomenon that governs hydrological cycles at the land-to-ocean transition zone. SGD manifests as cold and buoyant freshwater influx to the water column that contains carbon, nutrients, metals, and greenhouse gases, altering coastal areas' oceanographic~~al~~ and biochemical properties. This study presents electromagnetic imaging of large freshwater plumes in high-resolution, offshore west of Hawai'i island. Electrical resistivity models detect multiple vertical freshwater plumes extending from the seafloor to the ocean surface. Additionally, our models image extensive spatially distributed surface SGD. The resistivity of these freshwater plumes and surface SGD ranges from $\sim$1 to 30 Ωm. Our resistivity-to-salinity calculation presents a plume-scale salinity range of $\sim$0.3–9.9, containing up to 87% of freshwater. Thus, we suggest that substantial volumes of freshwater occupy water column plumes in Hawai'i. Our findings provide valuable information to elucidate hydrogeologic and oceanographic processes affecting biogeochemical cycles in coastal waters worldwide.

Plain Language Summary

Submarine groundwater discharge (SGD) is a flow of cold and buoyant freshwater from the seafloor the ocean surface. Because SGD contains carbon, nutrients, metals, and greenhouse gases, it changes the oceanographical and biochemical properties of coastal waters. Therefore, SGD is an important phenomenon that governs hydrological cycles at the land-to-ocean transition zone. Due to the high spatial distribution and variability of SGD at the ocean surface, it is nontrivial to map SGD seep location and fluxes using traditional oceanographic methods. Here, we present electromagnetic imaging of large freshwater plumes in high-resolution, offshore west of Hawai'i island. Our electrical resistivity models detect multiple vertical freshwater plumes (SGD point-sources) as well as spatially distributed surface SGD, extending to a distance of $\sim$3 km offshore Hawai'i. Plume-scale salinity distribution indicates that these plumes contain up to 87% of freshwater. Thus, a substantial volume of freshwater occupies Hawaiian water column plumes. Our findings provide valuable information to elucidate hydrogeologic and oceanographic processes affecting biogeochemical cycles in coastal waters worldwide. This is the first study to demonstrate the marine electromagnetic method's capability to image and delineate freshwater plumes from the seafloor to the ocean surface.

1 Introduction

Freshwater resources are essential for preserving public health, agricultural yields, economic strategies, and ecosystem functions (Gleick & Palaniappan, 2010; Michael et al., 2017). As populations and economies grow, new constraints on water resources emerge that may limit global water availability (Gleick & Palaniappan, 2010). Optimized groundwater systems' characterization and seeking alternative freshwater resources are vital to address the increasing demand worldwide. Hence, such demand positions groundwater research at the center of broad interdisciplinary interest from industry, government, and academic organizations (e.g. Person et al., 2017; Manzoor et al., 2020). For the past decade, considerable evidence suggests that vast offshore groundwater reserves exist globally in submarine provinces extending far beyond their presumed coastal boundaries (Post et al., 2013; Gustafson et al., 2019; Micallef et al., 2020). These offshore groundwater reservoirs are more prevalent than initially thought, thus are being recognized as potential water resources for coastal communities (Cohen et al., 2010; Bakken et al., 2012; Jiao et al., 2015).

Actively recharged offshore submarine groundwater domains frequently manifest by a process known as submarine groundwater discharge (SGD), where fresh groundwater percolates upward from the sub-seafloor to the water column, altering ocean water salinity, temperature, and chemistry (e.g. Church, 1996; Kohout, 1966; W. S. Moore, 2010). While coastal SGD has been documented globally at various geological settings (Stieglitz, 2005; Kim &

Kim, 2011; Knee et al., 2016; Prakash et al., 2018; Paldor et al., 2019), reports on deep sources of SGD are scarce but of potential importance. Fresh SGD is commonly associated with oceanographic, hydrogeological, and environmental processes affecting chemical weathering, ocean eutrophication, and climate change since it transports freshwater loaded with solutes and gases (e.g. W. S. Moore, 2010; Kim & Kim, 2011; Taniguchi et al., 2019; Luijendijk et al., 2020). Thus, SGD has societal importance for coastal communities (Moosdorf & Oehler, 2017). The locations and rates of nearshore/offshore SGD are essential to define boundary conditions in coastal aquifer models and characterize nutrients and contaminants transported to the marine environment (Duarte et al., 2006). The fresh portion of SGD is critical, as it potentially buffers ocean acidification with groundwater alkalinity (Slomp & Van Cappellen, 2004; Cyronak et al., 2013).

SGD is commonly studied using various geophysical, geochemical, bioecological, and numerical simulation methods, which utilize seepage meters and hydraulic gradient observations (e.g. Burnett et al., 2006; W. S. Moore, 2010; Taniguchi et al., 2019; Rosenberry et al., 2020). Nevertheless, it is nontrivial to produce regional SGD maps in high-resolution due to extensive spatiotemporal variability of flow, ranging from broad seepage fields to focused springs (Duarte et al., 2006; Burnett et al., 2006; Luijendijk et al., 2020). Therefore, high-resolution field characterizations of SGD on regional scales are rare. Thermal infrared imagery and geochemical tracer studies performed along the coast of west Hawaiʻi infer daily coastal groundwater discharge that varies between 1,100–13,700 m^3/d (Johnson et al., 2008; Peterson et al., 2009; Dulai et al., 2016). However, these studies only provide information about buoyant brackish/freshwater plumes emanating at the coastline, thus, neglecting offshore SGD. Therefore, offshore SGD locations, spatial plume distribution, and volumetric inventory from the seafloor to the ocean surface are poorly constrained offshore west of Hawaiʻi as well as globally.

Marine controlled-source electromagnetic (CSEM) methods have proven useful in imaging brackish/freshwater subsurface accumulations at sedimentary regions (e.g. Evans & Key, 2016; Haroon et al., 2018; Gustafson et al., 2019; Micallef et al., 2020), as they are sensitive to contrasts in bulk electrical resistivity resulting from alterations in pore water salinity (Edwards, 2005; S. Constable, 2010). However, CSEM data inversion has never been used to image freshwater plumes within the water column. Here, we employ a newly developed surface-towed CSEM system (Sherman et al., 2017) demonstrating for the first time the CSEM techniques' capability to image freshwater plumes in high-resolution on a local scale, as well as surface SGD on a regional scale, offshore west of Hawaiʻi. Additionally, we present plume-scale salinity distribution and freshwater volumetric estimation.

1.1 Geological and Oceanographical Setting

Extensive aquifers on the island of Hawaiʻi were formed consequently to volcanic eruptions during the initial building stage of each volcano (Gingerich & Oki, 2000). These volcanic eruptions are characterized by lava flows, faults, dikes, ash beds, lava tubes, and pyroclastic deposits, which formed the terrestrial aquifers situated on the island of Hawaiʻi (Oki, 1999; Gingerich & Oki, 2000). The abundance of lava tubes in this region increases the volcanic rocks' permeability, thereby promoting large aquifers (Oki, 1999; Gingerich & Oki, 2000). The shallow region offshore Hawaiʻi surveyed in this study (Figure 1) is composed of subaerial lava drapes, intermediately covered by coral reef terraces (J. G. Moore & Clague, 1987; Taylor, 2019), and low sediment content (see supporting information Figure S1). This volcanic formation enables the direct flow of submarine freshwater from the subsurface to the ocean.

SGD has a unique role in Hawaiʻi's ocean biogeochemistry, as it is the sole source of nutrients to the region oligotrophic coastal waters (Johnson et al., 2008). The continuous influx of SGD to the west of Hawaiʻi coastline results in nutrient-rich brackish mixtures of fresh and seawater (Johnson et al., 2008; Dimova et al., 2012; Dulai et al., 2016). North Pacific

Subtropical Gyre and Hawaiian archipelago interactions dominate the current dynamics in west Hawai'i via tidally-induced internal waves. The governing direction of these currents is along-shore with an average magnitude of 0.05–0.1 m/s (Janeković et al., 2013).

2 Methods

2.1 Data Acquisition and Processing

We collected marine CSEM data using a surface-towed CSEM system to image the electrical resistivity structure of the submerged flank of the Hualalai volcano (Attias et al., 2020), as well as the oceanic water column offshore west of Hawai'i. Our survey included towlines parallel and perpendicular to the Hualalai terrestrial aquifer at incremental distances from the Kailua-Kona coastline, covering an offshore region of about 4 km wide and 40 km long, producing $\sim$200 km of continuous CSEM data (Figure 1).

The surface-towed CSEM system employs a 40 m-long dipole antenna at $\sim$0.5 m behind the survey boat, towed at an average speed of 3.5 knots while transmitting a 100 A current. A doubly symmetric square waveform (Myer et al., 2011) at a fundamental frequency of 1 Hz with a sampling rate of 250 Hz generated a source dipole moment of 5.09 kAm (Attias et al., 2020). The survey boat surface-towed four broadband electromagnetic (EM) receivers at offsets 268, 536, 804, 1072 m. A Dorsal unit positioned 30 m behind the EM receivers array recorded the water depth and surface water conductivity/temperature. Each EM receiver recorded the inline horizontal electric field on a 2 m dipole positioned $\sim$0.65 m below the ocean surface. GPS units positioned above sea level (timing accuracy of 10 ns) and electronic compasses logged the receiver positions and orientations, respectively.

The acquired CSEM data were Fourier transformed into the frequency domain and stacked over 60 s intervals. This stacking corresponds to $\sim$20 m lateral distance between transmitter stack points, producing high-density amplitude and phase responses per receiver as a function of position and frequency harmonics. The stacked amplitude and phase responses were then merged with the transmitter's and receiver's navigational information. For the CSEM inversion, we used the strongest harmonics of the doubly symmetric square waveform (Myer et al., 2011), here corresponding to frequencies of 3 and 7 Hz. These two frequencies produced quality data and high sensitivity to the electrical resistivity of the water column. In combination with high data density, the frequencies yielded high-resolution inversion models.

2.2 CSEM Inversion Parameterization

To invert the CSEM data for electrical resistivity, we employed the open-source MARE2DEM code, a 2-D nonlinear regularized inversion method that uses a parallel goal-oriented adaptive finite-element algorithm (Key & Ovall, 2011; Key, 2016). MARE2DEM employs Occam's inversion, which searches for the smoothest model that fits the data to a predefined root-mean-square (RMS) target misfit (S. C. Constable et al., 1987). The CSEM inversion-starting model discretization includes a 10^{13} Ωm air layer as a fixed-parameter, followed by finely discretized (20 m $\times$ 10 m) quadrilateral mesh (Key, 2016) for the water column (free parameters with half-space resistivity of 0.2 Ωm), and fine mesh elements (1000 m $\times$ 10 m), defined as free parameters (half-space resistivity of 10 Ωm), as illustrated in supporting information Figure S2. A high-resolution multi-beam system recorded the bathymetry (supporting information Figure S1) used in the CSEM inversion modeling. The 40 m-long dipole transmitter and the 2 m-long towed EM receiver dipoles (Attias et al., 2020) were modeled as finite dipole lengths (Key, 2016). Our finite dipole inversions produced models with high sensitivity of the data to model parameters. The inversions' horizontal-to-vertical roughness varies between 2 and 10 as a function of a width-to-depth ratio. All of our CSEM inversion models fit the data to an RMS misfit of 1.0 with adequate model-to-data fits, yielding minimal and randomly distributed normalized residuals (see supporting information Figures S3 and S4).

2.3 Resistivity-to-Salinity Calculation

The electrical conductivity (inverse of electrical resistivity) derived from our CSEM inversion models were converted to salinity profiles (Figures 3b and 4b) using the Practical Salinity Scale 1978 (Lewis & Perkin, 1978). Salinity was calculated for each data point extracted from the resistivity models. We then filtered the data points for salinities <10, thus yielding cells representing freshwater plume solely. By employing a 2-component mixing formula, we calculated the total volume of freshwater in each cell using Equation 1.

$$f1 \times sal1 + f2 \times sal2 = Sal\_mixed \tag{1}$$

Where $f1$ represents the volumetric fraction of pure freshwater, $f2$ the volumetric fraction of pure ocean water, $sal1$ the salinity of the pure freshwater (assuming it equals to 0.1), $sal2$ the salinity of the pure ocean water (assuming it equals to 35), and Sal_mixed is the calculated mixed salinity.

The resistivity-to-salinity conversion method applied here is theoretically robust. However, this method is limited in regions where the resistivity values are significantly small or significantly large. As resistivity values proceed towards minimal values, the resulting conductivities and thus salinities, approach infinity (see supporting information Figure S5). While measured resistivities cannot be zero, the step size effectively limits the method's ability to distinguish between different salinity values above ∼10. Therefore, we chose 0.58 Ωm (salinity of 10) as the method lower sensitivity limit, as it represents the point in the resistivity-salinity curve where the salinity change per unit of resistivity change nears a vertical slope (supporting information Figure S5). Because of this relationship, salinities within a range of 11–35 cannot be distinguished. Consequently, regions with salinity more than 10 were not calculated for the CSEM inversion models of survey lines 3a and 3d.

3 Results

The electrical resistivity structure of the sub-seafloor offshore west of Hawai'i using all the survey lines shown in Figure 1 has been previously characterized by Attias et al. (2020). Here, we focus on 2-D isotropic CSEM inversion modeling of the water column using data collected at four sections of survey line 3 (Figure 1). Our CSEM models image electrically resistive freshwater plumes in high-resolution and detect spatially distributed anomalous resistive regions at the ocean surface, indicative of large freshwater bodies (Figures 2–4). The Jacobian sensitivity matrix (Farquharson & Oldenburg, 1996; MacGregor et al., 2001) derived from our inversion models demonstrate high data sensitivity to model parameters across the entire water column.

3.1 Electromagnetic Imaging of Freshwater Plumes

Survey line 3b (located ∼2 km from the coastline) electrical resistivity model presents a vertical feature with varying resistivity, ranging from ∼2 Ωm near the seafloor to ∼25 Ωm at the ocean surface (Figure 2a). We interpret this vertical resistor as a freshwater water plume because the ocean's background resistivity is ∼0.2–0.4 Ωm. This freshwater plume is ∼60 m wide at the seafloor and ∼130 m at the surface. From both flanks of the model, two laterally elongated resistive anomalies (∼30 Ωm) extend from the surface to a depth of ∼15 m, indicating the presence of surface freshwater. These two surface freshwater bodies most likely emerge from nearby discharge points or extend from the coastal region, as they are disconnected from Line 3b plume (Figure 2a). The model-to-data fit and normalized residuals of line 3b inversion are shown in supporting information Figure S3.

Similar to the electrical resistivity model of survey line 3b, the resistivity model of survey line 3c exhibits a central vertically elongated freshened (moderately brackish) water plume, with a resistivity range of ∼1–5 Ωm from the seafloor to the ocean surface, respectively (Figure 2b). This plume is ∼100 m wide at the seafloor and ∼80 m at the surface. Additionally, two laterally extensive surface freshwater bodies were detected, showing resistivity of ∼30 Ωm (Figure 2b). The surface freshwater body at the northwest flank of the model is disconnected from the plume. However, the southeast surface freshwater body is moderately linked to the plume, presenting a six times higher resistivity than the plume's surface resistivity (Figure 2b). This suggests the southeast surface freshwater body accumulates freshwater mostly from nearby discharge points and possibly, a minor influx from line 3c plume. Supporting information Figure S4 shows the model-to-data fit and normalized residuals of line 3c inversion.

The electrical resistivity model of survey line 3a (located ∼2.3 km from the coastline) shows a freshened water plume (∼2.5 Ωm) that traverses the water column (Figure 3a). This plume is ∼100 m wide at the seafloor and ∼20 m at the surface. Figure 3a ideally demonstrates that a sub-seafloor freshened water layer (Attias et al., 2020) feeds this plume.

The electrical resistivity model of survey line 3d (located 0.5–1 km from the coastline) presents a prominent freshwater plume that is laterally extensive (∼200 m wide) above the seafloor and at the ocean surface but narrow at its center (Figure 4a). The plume's highest resistivity (∼30 Ωm) is between the surface and ∼25 m water depth, whereas near the seafloor, the water resistivity is ∼5 Ωm. The sub-seafloor freshened water layer (Attias et al., 2020) and the water column plume appear to be linked. However, the high resistivity detected near the ocean surface might also result from nearby discharge locations. At the northwest flank of the model, ∼30 Ωm resistive anomaly exists between the surface and ∼15 m depth, extending horizontally about 230 m (Figure 4a). This surface freshwater body is disconnected from line 3d plume, representing freshwater flux from a nearby seafloor and drifting into line 3d profile.

3.2 Plume salinity distribution and freshwater volumetric estimation

We calculated the water column salinity distribution and freshwater volumetric estimation for the plumes imaged by the electrical resistivity models of survey lines 3a and 3d (Figures 3a and 4a). For this purpose, we used the unitless Practical Salinity Scale 1978 (Lewis & Perkin, 1978) to derive water column salinities that are less than 10 (see section 2.3). The salinity distribution of line 3a plume region (308 m long by 83 m deep, Figure 3b) was calculated using 6,204 points (represented as model cells). The total unit volume of the profile is 23,400 m^3. Note that unit volume refers to a profile thickness of 1 m. Salinities less than 10 were found in 1,778 model cells, representing a plume unit volume of 7,473 m^3. The inner plume calculated salinities ranged from 0.5 to 9.85 (Figure 3b), with an average salinity of 5.3. By applying the 2-component mixing equation (section 2.3), we computed that the total freshwater unit volume for line 3a inner plume area is 6,350 m^3. Such volume equates to a plume composition of about 85% freshwater, and 15% ocean water.

The salinity distribution of line 3d plume region (206 m long by 83 m deep, Figure 4b) was calculated using 4,242 points. The total unit volume of the profile is 17,100 m^3. Salinities less than 10 were found in 2,762 model cells, representing a plume unit volume of 12,280 m^3. The inner plume calculated salinities ranged from 0.3 to 9.88 (Figure 4b), with an average salinity of 4.4. The total calculated freshwater unit volume for line 3d inner plume area is 10,720 m^3, composed of approximately 87% freshwater and 13% ocean water.

4 Discussion

Global utilization of sizeable submarine freshwater reserves can mitigate the adverse effects of onshore pumping, commonly manifested by seawater intrusion, thus ideally, expanding the hydrological boundaries towards the offshore domain (Galloway & Burbey, 2011; Bakken et al., 2012; Ferguson & Gleeson, 2012; Post et al., 2013). Terrestrial aquifers are one of Hawai'i's most critical natural resources, providing the majority of water for drinking, irrigation, domestic, commercial, and industrial needs (Gingerich & Oki, 2000). Due to forecasted decreases in rainfall at areas under existing climate change projections (Timm et al., 2015; Zhang et al., 2016), increase in population, and agricultural demands on the island of Hawai'i, it is essential to explore new viable alternative sources of freshwater.

Multiple point-source SGD locations offshore west of Hawai'i are likely linked to inland lava flow formations (Peterson et al., 2009; Dimova et al., 2012), manifested by subsurface laterally continuous freshened groundwater reservoirs (Attias et al., 2020). Multichannel electrical resistivity measurements (Dimova et al., 2012) provide evidence for substantial coastal SGD via well-defined freshwater conduits in Kiholo Bay, northwest of our study region (Figure 1). Calculation of SGD rates at Kiholo Bay from surface thermal infrared imagery and point-source measurements suggests a total discharge that averages between 8,600–9,600 m^3/d (Johnson et al., 2008; Dimova et al., 2012; Dulai et al., 2016). Such discharge values are comparable with our estimation of the plumes unit volumes described above. Hence, substantial SGD volumes are required to produce such sharply bounded, well-defined large freshened/freshwater plumes (Figures. 2–4), despite the dynamic current field in the study region that generates effective mixing (Janeković et al., 2013). These observations suggest that the offshore submarine freshened water layers (Attias et al., 2020), are most likely renewable sources of water. This is supported by a water mass balance study (Hudson et al., 2018), which demonstrates that significant fresh groundwater recharge/discharge volumetric misbalance ($\sim$40%) exists between the Hualalai aquifer groundwater recharge and SGD along the corresponding Kailua-Kona coastline.

As the discharge locations and rates of freshwater are highly heterogeneous, spatiotemporal estimates of SGD are essential for better managing water resources and predicting water quality threats at coastal aquifers, land-ocean boundary, and oceanic surface waters (Sawyer et al., 2016). Our regional-scale electromagnetic mapping offshore west of Hawai'i shows the precise location of several individual SGD plumes and their spatial distribution from the seafloor to the ocean surface. This provides evidence of a complex hydrogeologic setting of multiple interbedded volcanic layers that channel fresh groundwater to deeper layers, allowing freshwater to discharge at a significant distance from the coastline. Electromagnetic imaging ability to map and quantify deep offshore freshwater discharges is a powerful tool to assess SGD fluxes' effects on marine biochemistry on localized and regional scales.

5 Conclusions and Implications

Spatiotemporal variability of fresh SGD in coastal waters alters oceanographic, hydrogeologic, and biogeochemical processes, promoting ocean eutrophication and climate change. Various geophysical, geochemical, and bioecological studies suggest that SGD in west Hawai'i is distributed across a large regional-scale. Our marine electromagnetic imaging reveals multiple offshore SGD plumes, most likely fed by freshened water submarine accumulations. Plume-scale resistivity-to-salinity calculation and volumetric estimation infer that significant freshwater volumes accommodate these water column plumes. Utilization of the submarine renewable freshened water bodies linked to freshwater plumes can significantly increase water availability to the island of Hawai'i. This is the first study to demonstrate the CSEM method's capability to image and delineate freshwater plumes from the seafloor to the ocean surface in high-resolution. Thus, oceanographic, hydrogeologic, and biogeochemical studies can use marine CSEM to characterize complex, large-scale coastal water processes worldwide.

Acknowledgments
This study was supported via the Hawai'i EPSCoR Program, funded by the National Science

Foundation Research Infrastructure Improvement Award (RII) Track-1: ‘Ike Wai: Securing Hawai‘i's Water Future Award # OIA-1557349. The authors would like to thank G. Jacobs, B. Taylor, N. Maximenko, B. Powell, and I. H. Falcon-Suarez for helpful discussions. We also thank the scientific party of survey boat Huki Pono and the Natural Energy Laboratory of Hawaii Authority for survey support. The CSEM data is available for download at `https://doi.org/10.4211/hs.e0a7f2a216e9456a8567b850db1cf1f9`.

References

Attias, E., Thomas, D., Sherman, D., Ismail, K., & Constable, S. (2020). Marine electrical imaging reveals novel freshwater transport mechanism in Hawai‘i. *Science Advances*, *6*(48), eabd4866.

Bakken, T. H., Ruden, F., & Mangset, L. E. (2012). Submarine groundwater: a new concept for the supply of drinking water. *Water Resour. Manage.*, *26*(4), 1015–1026.

Burnett, W., Aggarwal, P., Aureli, A., Bokuniewicz, H., Cable, J., Charette, M., ... others (2006). Quantifying submarine groundwater discharge in the coastal zone via multiple methods. *Sci. Total Environ.*, *367*(2-3), 498–543.

Church, T. M. (1996). An underground route for the water cycle. *Nature*, *380*(6575), 579–580.

Cohen, D., Person, M., Wang, P., Gable, C. W., Hutchinson, D., Marksamer, A., ... others (2010). Origin and extent of fresh paleowaters on the Atlantic continental shelf, USA. *Groundwater*, *48*(1), 143–158.

Constable, S. (2010). Ten years of marine CSEM for hydrocarbon exploration. *Geophysics*, *75*(5), 67–81.

Constable, S. C., Parker, R. L., & Constable, C. G. (1987). Occam's inversion: A practical algorithm for generating smooth models from electromagnetic sounding data. *Geophysics*, *52*(3), 289-300.

Cyronak, T., Santos, I. R., Erler, D. V., & Eyre, B. D. (2013). Groundwater and porewater as major sources of alkalinity to a fringing coral reef lagoon (Muri Lagoon, Cook Islands). *Biogeosciences*, *10*(4), 2467.

Dimova, N. T., Swarzenski, P. W., Dulaiova, H., & Glenn, C. R. (2012). Utilizing multichannel electrical resistivity methods to examine the dynamics of the fresh water–seawater interface in two Hawaiian groundwater systems. *J. Geophys. Res.*, *117*(C2), 10.1029/2011JC007509.

Duarte, T. K., Hemond, H. F., Frankel, D., & Frankel, S. (2006). Assessment of submarine groundwater discharge by handheld aerial infrared imagery: Case study of Kaloko fishpond and bay, Hawai‘i. *Limnol. Oceanogr.*, *4*(7), 227–236.

Dulai, H., Kamenik, J., Waters, C. A., Kennedy, J., Babinec, J., Jolly, J., & Williamson, M. (2016). Autonomous long-term gamma-spectrometric monitoring of submarine groundwater discharge trends in Hawaii. *J. Radioanal. Nucl. Chem*, *307*(3), 1865–1870.

Edwards, N. (2005). Marine controlled source electromagnetics: principles, methodologies, future commercial applications. *Surv. Geophys.*, *26*(6), 675–700.

Evans, R., & Key, K. (2016). Mapping Offshore Freshwater Deposits Using Electromagnetic Methods. In *Near surface geoscience 2016 - second applied shallow marine geophysics conference* (p. 10.3997/2214-4609.201602169).

Farquharson, C., & Oldenburg, D. (1996). Approximate sensitivities for the electromagnetic inverse problem. *Geophys. J. Int.*, *126*(1), 235–252.

Ferguson, G., & Gleeson, T. (2012). Vulnerability of coastal aquifers to groundwater use and climate change. *Nature Clim. Change*, *2*(5), 342.

Galloway, D. L., & Burbey, T. J. (2011). Regional land subsidence accompanying groundwater extraction. *Hydrogeol. J.*, *19*(8), 1459–1486.

Gingerich, S. B., & Oki, D. S. (2000). *Ground water in hawaii* (Vol. 126; Tech. Rep.). US Geological Survey.

Gleick, P. H., & Palaniappan, M. (2010). Peak water limits to freshwater withdrawal and use. *Proceedings of the National Academy of Sciences*, *107*(25), 11155–11162.

Gustafson, C., Key, K., & Evans, R. L. (2019). Aquifer systems extending far offshore on the US Atlantic margin. *Sci. Rep.*, *9*(1), 1–10.

Haroon, A., Lippert, K., Mogilatov, V., & Tezkan, B. (2018). First application of the marine differential electric dipole for groundwater investigations: A case study from Bat Yam, Israel. *Geophysics*, *83*(2), B59–B76.

Hudson, C., Dulai, H., & El-Kadi, A. (2018). Determining flow paths of submarine groundwater discharge on the kona cost, hawai'i. In *Ocean sciences meeting, portland, oregon.*

Janeković, I., Powell, B., Matthews, D., McManus, M., & Sevadjian, J. (2013). 4D-Var data assimilation in a nested, coastal ocean model: A Hawaiian case study. *J. Geophys. Res.*, *118*(10), 5022–5035.

Jiao, J. J., Shi, L., Kuang, X., Lee, C. M., Yim, W. W.-S., & Yang, S. (2015). Reconstructed chloride concentration profiles below the seabed in Hong Kong (China) and their implications for offshore groundwater resources. *Hydrogeol. J.*, *23*(2), 277–286.

Johnson, A. G., Glenn, C. R., Burnett, W. C., Peterson, R. N., & Lucey, P. G. (2008). Aerial infrared imaging reveals large nutrient-rich groundwater inputs to the ocean. *Geophys. Res. Lett.*, *35*(15).

Key, K. (2016). MARE2DEM: a 2-D inversion code for controlled-source electromagnetic and magnetotelluric data. *Geophys. J. Int.*, *207*(1), 571–588.

Key, K., & Ovall, J. (2011). A parallel goal-oriented adaptive finite element method for 2.5-D electromagnetic modelling. *Geophys. J. Int.*, *186*(1), 137-154.

Kim, I., & Kim, G. (2011). Large fluxes of rare earth elements through submarine groundwater discharge (SGD) from a volcanic island, Jeju, Korea. *Mar. Chem.*, *127*(1-4), 12–19.

Knee, K. L., Crook, E. D., Hench, J. L., Leichter, J. J., & Paytan, A. (2016). Assessment of submarine groundwater discharge (SGD) as a source of dissolved radium and nutrients to Moorea (French Polynesia) coastal waters. *Estuar. Coast.*, *39*(6), 1651–1668.

Kohout, F. (1966). Submarine springs: a neglected phenomenon of coastal hydrology. *Hydrology*, *26*, 391–413.

Lewis, E. L., & Perkin, R. (1978). Salinity: Its definition and calculation. *J. Geophys. Res.*, *83*(C1), 466–478.

Luijendijk, E., Gleeson, T., & Moosdorf, N. (2020). Fresh groundwater discharge insignificant for the worlds oceans but important for coastal ecosystems. *Nat. Commun.*, *11*(1), 1–12.

MacGregor, L., Sinha, M., & Constable, S. (2001). Electrical resistivity structure of the Valu Fa Ridge, Lau Basin, from marine controlled-source electromagnetic sounding. *Geophys. J. Int.*, *146*(1), 217-236.

Manzoor, Q., Martin-Nagle, R., Oster, J., Lamizana, B., Voutchkov, N., KooOshimma, S., ... Person, M. (2020). UN-Water, 2020: UN-Water Analytical Brief on Unconventional Water Resources. Geneva, Switzerland.

Micallef, A., Person, M., Haroon, A., Weymer, B. A., Jegen, M., Schwalenberg, K., ... others (2020). 3D characterisation and quantification of an offshore freshened groundwater system in the Canterbury Bight. *Nat. Commun.*, *11*(1), 1–15.

Michael, H. A., Post, V. E., Wilson, A. M., & Werner, A. D. (2017). Science, society, and the coastal groundwater squeeze. *Water Resour. Res.*, *53*(4), 2610–2617.

Moore, J. G., & Clague, D. (1987). Coastal lava flows from Mauna Loa and Hualalai volcanoes, Kona, Hawaii. *Bull. Volcanol.*, *49*(6), 752–764.

Moore, W. S. (2010). The effect of submarine groundwater discharge on the ocean. *Annu. Rev. Mar. Sci.*, *2*, 345–347.

Moosdorf, N., & Oehler, T. (2017). Societal use of fresh submarine groundwater discharge: An overlooked water resource. *Earth-Sci. Rev.*, *171*, 338–348.

Myer, D., Constable, S., & Key, K. (2011). Broad-band waveforms and robust processing for marine CSEM surveys. *Geophys. J. Int.*, *184*(2), 689–698.

Oki, D. S. (1999). *Geohydrology and numerical simulation of the ground-water flow system of Kona, island of Hawaii* (Vol. 70; Tech. Rep.). Geological Survey (US).

Paldor, A., Katz, O., Aharonov, E., Weinstein, Y., Roditi-Elasar, M., Lazar, A., & Lazar, B. (2019). Deep submarine groundwater discharge–Evidence from Achziv Submarine Canyon at the exposure of the Judea Group confined aquifer, eastern Mediterranean. *J. Geophys. Res.*.

Person, M., Wilson, J. L., Morrow, N., & Post, V. E. (2017). Continental-shelf freshwater water resources and improved oil recovery by low-salinity waterflooding. *AAPG Bulletin*, *101*(1), 1–18.

Peterson, R. N., Burnett, W. C., Glenn, C. R., & Johnson, A. G. (2009). Quantification of point-source groundwater discharges to the ocean from the shoreline of the Big Island, Hawaii. *Limnology and Oceanography*, *54*(3), 890–904.

Post, V. E., Groen, J., Kooi, H., Person, M., Ge, S., & Edmunds, W. M. (2013). Offshore fresh groundwater reserves as a global phenomenon. *Nature*, *504*(7478), 71.

Prakash, R., Srinivasamoorthy, K., Gopinath, S., & Saravanan, K. (2018). Measurement of submarine groundwater discharge using diverse methods in Coleroon Estuary, Tamil Nadu, India. *Appl. Water Sci.*, *8*(1), 13.

Rosenberry, D. O., Duque, C., & Lee, D. R. (2020). History and evolution of seepage meters for quantifying flow between groundwater and surface water: Part 1–Freshwater settings. *Earth-Sci Rev.*, 103167.

Sawyer, A. H., David, C. H., & Famiglietti, J. S. (2016). Continental patterns of submarine groundwater discharge reveal coastal vulnerabilities. *Science*, *353*(6300), 705–707.

Sherman, D., Kannberg, P., & Constable, S. (2017). Surface towed electromagnetic system for mapping of subsea Arctic permafrost. *Earth Planet. Sci. Lett.*, *460*, 97–104.

Slomp, C. P., & Van Cappellen, P. (2004). Nutrient inputs to the coastal ocean through submarine groundwater discharge: controls and potential impact. *J. Hydrol.*, *295*(1-4), 64–86.

Stieglitz, T. (2005). Submarine groundwater discharge into the near-shore zone of the Great Barrier Reef, Australia. *Mar. Pollut. Bull.*, *51*(1-4), 51–59.

Taniguchi, M., Dulai, H., Burnett, K. M., Santos, I. R., Sugimoto, R., Stieglitz, T., ... Burnett, W. (2019). Submarine Groundwater Discharge: Updates on its Measurement Techniques, Geophysical Drivers, Magnitudes and Effects. *Front. Environ. Sci.*, *7*, 141.

Taylor, B. (2019). Shoreline slope breaks revise understanding of Hawaiian shield volcanoes evolution. *Geochem. Geophys. Geosyst.*, *20*(8), 4025–4045.

Timm, O. E., Giambelluca, T. W., & Diaz, H. F. (2015). Statistical downscaling of rainfall changes in Hawaiʻi based on the CMIP5 global model projections. *J. Geophys. Res.*, *120*(1), 92–112.

Zhang, C., Wang, Y., Hamilton, K., & Lauer, A. (2016). Dynamical downscaling of the climate for the Hawaiian Islands. Part I: Present day. *J. Clim.*, *29*(8), 3027–3048.

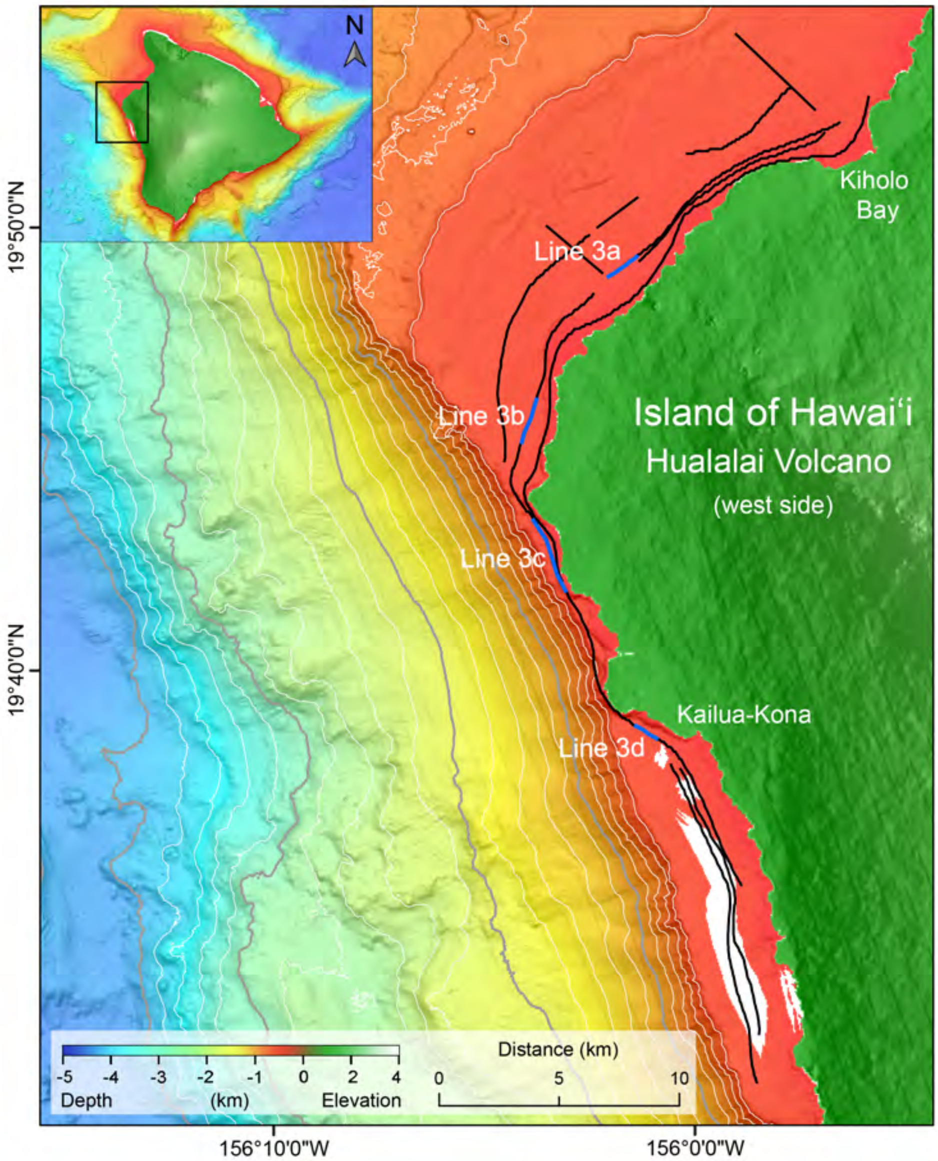

Figure 1. Map of the study area parallels the Hualalai terrestrial aquifer at Kailua-Kona, offshore west of Hawai'i. The black lines denote the survey towlines (10 inlines, and two crosslines). Blue lines represent regions where freshwater plumes were detected (Figures 2–4). White lines denote depth contours of 200 m, and grey lines the depth contours of 1000 m. Inset map: The island of Hawai'i, with a black rectangle indicating the main map area. Areas with no bathymetry data are shown in white. Bathymetry data: Courtesy of Hawai'i Mapping Research Group.

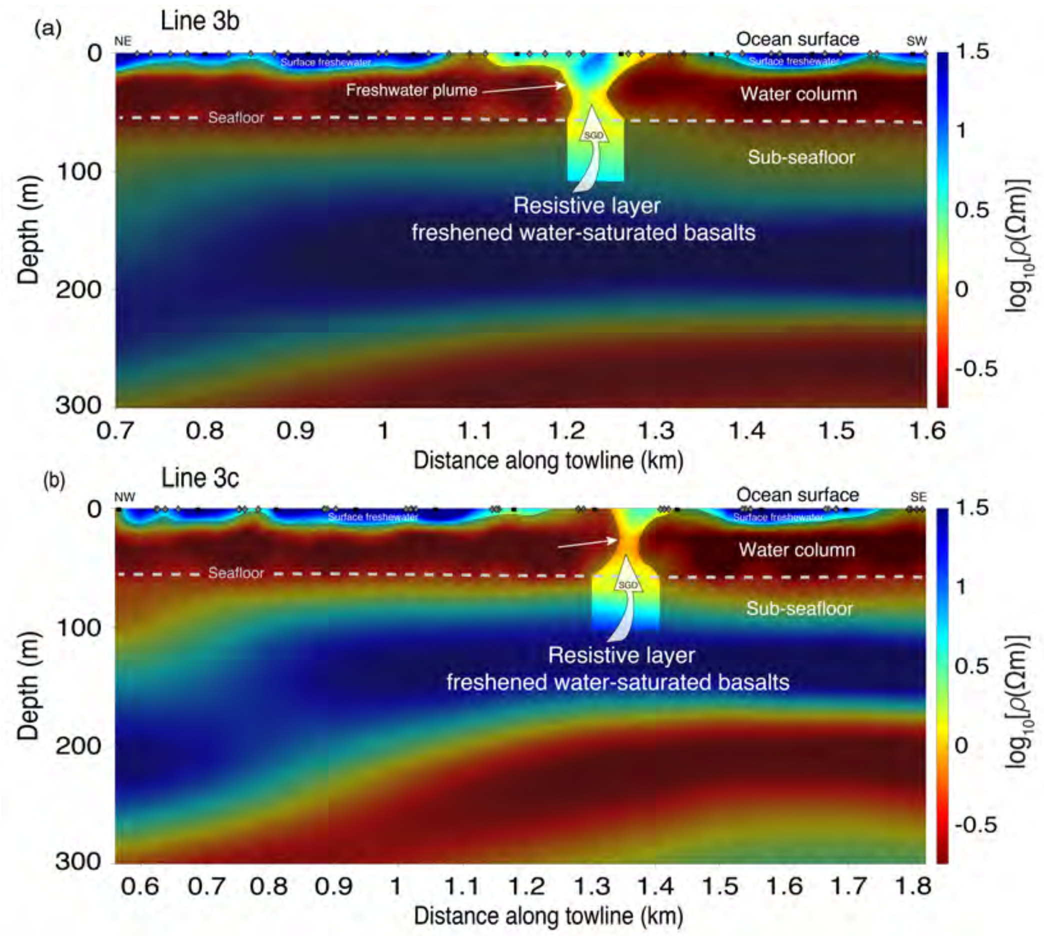

Figure 2. Two-dimensional inversion models derived from the CSEM data acquired in survey lines 3b and 3c. The color scale presents the electrical resistivity in $\log_{10}[\rho(\Omega\text{m})]$. Black squares and grey diamonds denote transmitter and receiver positions, respectively. We note that for enhanced visuality of the water column resistive anomalies, the resistivity shading thresholds are set to $\geqslant 1$ Ωm and $\geqslant 6$ Ωm for the plume and surface freshwater bodies, respectively. (a) Line 3b inversion model. The grey dashed line represents the seafloor, positioned at a water depth of $\sim$50 m. Resistive freshwater plume imaged at a towline distance of $\sim$1.23 km. The plume is most likely fed by SGD (white arrow) sourced from the sub-seafloor layer of freshened water-saturated basalts. Two lateral resistive anomalies from both flanks of the model represent surface freshwater bodies. This inversion converged to an RMS misfit of 1.0 after 12 iterations. The amplitude and phase data error floors are 8%. (b) Line 3c inversion model. Moderate freshwater plume detected at a towline distance of $\sim$1.35 km. The shallow lateral resistive anomalies represent surface freshwater bodies. This inversion fit to an RMS misfit of 1.0 after 14 iterations, with error floors of 8% and 6% for the amplitude and phase data, respectively.

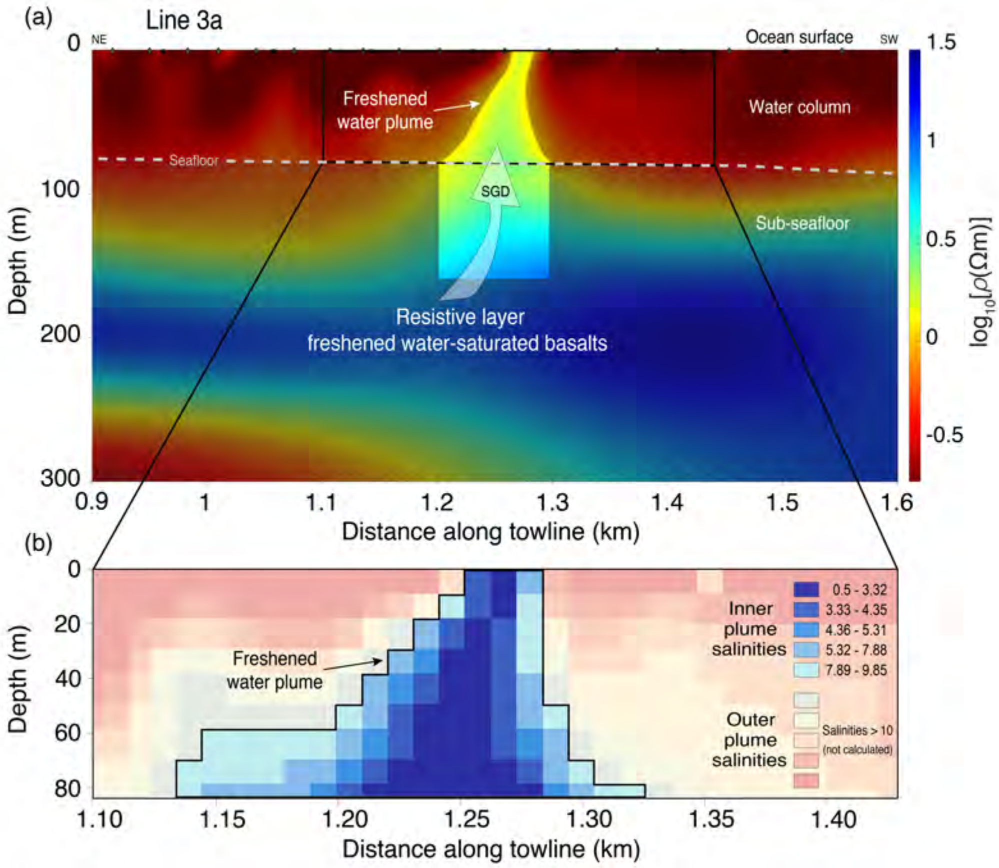

Figure 3. (a) Two-dimensional inversion model derived from the CSEM data acquired in survey line 3a. The color scale presents the electrical resistivity in $\log_{10}[\rho(\Omega\text{m})]$. The grey dashed line represents the seafloor, positioned at a water depth of ~85 m. The water column resistivity shading threshold is $\geqslant$1.7 Ωm. Resistive freshened water plume imaged at a towline distance of ~1.25 km. The inversion converged to an RMS of 1.0 after 19 iterations. The amplitude and phase data error floors are 10%. Black rectangular represents the plume area selected for salinity calculation. (b) Line 3a water column salinity distribution. The black line encompasses low salinities (<10) within the plume, calculated from the resistivity model. The average plume salinity is 5.3, with ~85% of freshwater. Salinities outside the plume were not calculated (see section 2.3).

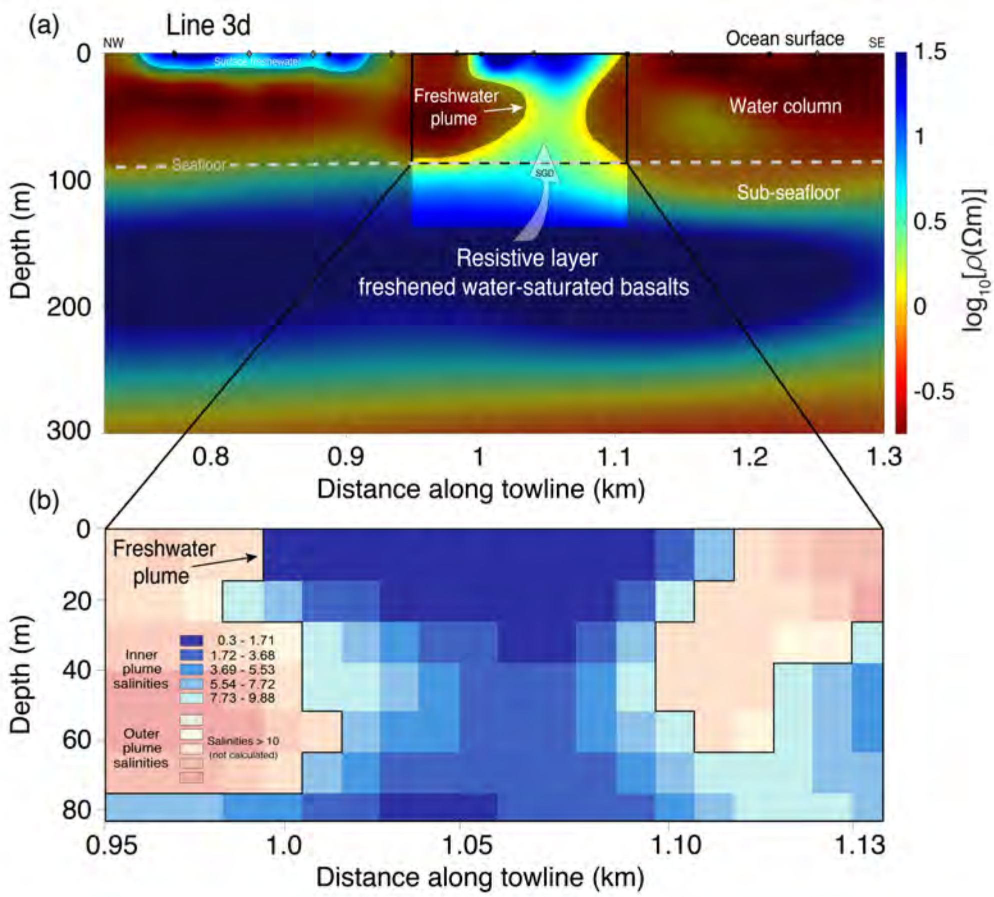

Figure 4. (a) Two-dimensional inversion model derived from the CSEM data acquired in survey line 3d. The color scale presents the electrical resistivity in $\log_{10}[\rho(\Omega\mathrm{m})]$. The grey dashed line represents the seafloor, positioned at a water depth of ~95 m. For enhanced visuality of the water column resistive anomalies, the resistivity shading thresholds are $\geqslant$1.7 Ωm and $\geqslant$6 Ωm for the plume and surface freshwater body, respectively. Distinctive freshwater plume imaged at a towline distance of ~1–1.1 km. This inversion converged to an RMS of 1.0 after 15 iterations, with error floors of 9% and 7% for the amplitude and phase data, respectively. Black rectangular represents the water column plume area selected for salinity calculation. (b) Line 3d water column salinity distribution. The black line encompasses low salinities (<10) within the plume, calculated from the resistivity model. The average plume salinity is 4.4, with ~87% of freshwater. Salinities outside the plume were not calculated (see section 2.3).